

High efficiency co-sensitized solar cell based on luminescent lanthanide complexes with pyridine-2,6-dicarboxylic acid ligands†

Xin Wang,^{a,b} Yu-Lin Yang,^{*a} Ping Wang,^a Liang Li,^a Rui-Qing Fan,^{*a} Wen-Wu Cao,^c Bin Yang,^c Hui Wang^d and Jing-Yao Liu^d

Received 22nd February 2012, Accepted 17th June 2012

DOI: 10.1039/c2dt30430a

Two lanthanide complexes, Ln(HPDA)₃·4EtOH (Ln = Tb, Dy) (H₂PDA = pyridine-2,6-dicarboxylic acid, EtOH = ethanol), have been successfully synthesized using hydrothermal or solvothermal methods, and their crystal structures were analyzed by single crystal XRD. Both crystals have orthorhombic symmetry with space group *Pbcn*, exhibiting three-dimensional (3D) supramolecular architecture through hydrogen bonding interactions. The metal center was coordinated to nine atoms by three pyridine-2,6-dicarboxylic acid ligands. The nine-coordinated lanthanide metal complexes were assembled onto a nanocrystalline TiO₂ film to form co-sensitized photoelectrodes with N719 for dye-sensitized solar cells, and their photoelectrochemical performance was studied. In the tandem structure of composite electrodes, the energy levels of lanthanide metal complexes are reorganized in their single-crystal form, as verified by *ab initio* calculations. The co-sensitized systems are far superior for electron-injection and hole-recovery compared with single N719-sensitized systems. Luminescence properties were measured and electrochemical analysis was also performed on these complexes.

Introduction

Since O'Regan and Grätzel pioneered the field of dye-sensitized solar cells (DSSCs) in 1991,¹ scientists have shown great enthusiasm in developing new sensitizers that can lead to higher incident photon-to-electron conversion efficiency (IPCE) over a substantially wider band of wavelengths by molecular engineering. However, for most new sensitizers, optimization to give a high IPCE value and a broad absorption band involves some degree of trade-off. In order to improve the absorption ability of a solar cell, co-sensitization by means of multiple sensitizers would appear to be more achievable.^{2,3} However, unfavorable interactions between different types of dye molecules often decreases photovoltaic performance. Therefore, in recent years, the arrangement of micro- and nanostructured building blocks has gained popularity.⁴ Inorganic dyes offer a lot of possibilities for improving a wide range of properties, such as molecular structure and function, efficient light-harvesting ability in

different parts of the solar spectrum, controllable molecular energy levels, charge generation and separation, and molecule-to-molecule interactions. They can easily be designed to absorb light more effectively, so that thinner films can be used to generate an optimal photovoltaic effect. Although advances have been made with metal-coordination dyes as sensitizers in DSSCs, there is still a need to optimize their chemical and physical properties to further improve the performance of solar cells. The co-sensitization with multiple dyes is very appealing for obtaining panchromatic absorption, but perfect tuning is quite difficult to achieve. Ehret *et al.* studied the nanocrystalline TiO₂ solar cell sensitized by various dicarboxylated cyanines and found that the use of mixed cyanine dyes could improve photoelectric conversion efficiency.⁵ Zhang and coworkers examined the mechanism of the co-sensitization with squarylium and N3 dyes by time-resolved spectroscopy.⁶ Grätzel and coworkers combined bithiophene dye (JK2) with squarylium cyanine dye (SQ1) as co-sensitizers and achieved an overall conversion efficiency as high as 7.43%.⁷ This value is so far the highest value reported for co-sensitized DSSCs with metal-coordination organic dyes. Recently, Wang *et al.* reported that the enhanced performance of chlorophyll-sensitized solar cells have been obtained by co-sensitization of a-type Chl with b-, or c-type Chl.⁸

On the other side, trivalent rare earth doped semiconductors are technologically important materials in optoelectric devices and have received a lot of attention,⁹ in which an efficient energy transfer from semiconductor host to RE ions is essential for most potential applications. Unfortunately, the doping of RE ions into the crystal structure of semiconductors remains unsuccessful.¹⁰ The difficulty is due to the inappropriate energy level

^aDepartment of Applied Chemistry, Harbin Institute of Technology, Harbin 150001, P.R. China. E-mail: fanruqing@hit.edu.cn, ylyang@hit.edu.cn; Fax: +86 451 86418270; Tel: +86 451 86413710

^bDepartment of Food and Environmental Engineering, Heilongjiang East University, Harbin 150086, P.R. China

^cCondensed Matter Science and Technology Institute, Harbin Institute of Technology, Harbin 150001, P.R. China

^dInstitute of Theoretical Chemistry, State Key Laboratory of Theoretical and Computational Chemistry, Jilin University, Changchun 130023, P.R. China

† Electronic supplementary information (ESI) available. CCDC 740890 and 818568. For ESI and crystallographic data in CIF or other electronic format see DOI: 10.1039/c2dt30430a

position of rare earth ions relative to the valence band and conduction band of the semiconductor host. To optimize the matching of energy band structure with TiO_2 in solar cells, we designed a series of lanthanide complex sensitizers with 4f structure. In the research of coordination complexes constructed by carboxylate ligands, the focus has been on lanthanide and transition metal coordination complexes constructed by multi-carboxylate ligands, such as benzene-1,2,4,5-tetracarboxylate, benzene-1,3,5-tricarboxylate, pyridine-2,3(5)-dicarboxylate and pyridine-2,6-dicarboxylate.^{11–16} These multi-carboxylate ligands possess interesting features that can facilitate the formation of versatile coordination structures. Owing to steric hindrance, the multi-carboxylate groups on the molecules may be completely or partially deprotonated and the carboxylate groups may not lie in the phenyl and pyridine ring plane upon coordination to metal ions. As a result, the molecules may connect metal ions in different directions, generating multidimensional architectures.¹⁷

In this work, we selected two lanthanide complexes, whose crystal structures have not been reported, as co-sensitizers for the study of photoelectrochemical properties in dye-sensitized solar cells. The relationships among molecule structures, photoluminescent and electrochemical properties have also been investigated. This is the first time that lanthanide complexes based on pyridine-2,6-dicarboxylic acid ligands have co-sensitized photoanodes of TiO_2 to form composite photoelectrodes with N719. According to the *ab initio* calculations, the complexes play an important role in the optimization matching with dyes in the compounds for increasing electrical conversion efficiency.

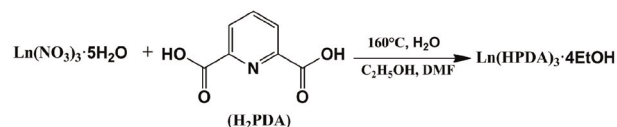
Experimental section

Synthesis of lanthanide complexes

All reagents were commercially available and used without further purification. The pyridine-2,6-dicarboxylic acid was prepared by oxidation reaction from 2,6-dimethylpyridine. 2,6-Dimethylpyridine (20 mL, 0.17 mol) was added into 500 mL water and potassium permanganate (54.4 g, 0.34 mol) was slowly added to the solution. Then the solution was heated to 25 °C and maintained for 2 h until the disappearance of the purple color. Further potassium permanganate (54.4 g, 0.34 mol) and water (300 mL) was slowly added and the mixture was again heated and maintained at 25 °C. After 2–3 h, the purple color disappeared again. Afterwards, the reaction solution was cooled to room temperature. Repeat filtration and removal of solvent was carried out until the residual volume was reduced to ~200 mL. Then sulfuric acid (70%, 35 mL) was added slowly and the precipitate was filtered to yield pyridine-2,6-dicarboxylic acid as a white solid (20.62 g, yield: 71.8%). Mp: 220.1–221.3 °C. IR (KBr, cm^{-1}): 3456(m), 3070(m), 1704(vs), 1575(m), 1460(m), 1416(m), 1331(m), 1300(m), 1267(s), 1163(w), 1082(w), 997(w), 927(w), 753(w), 702(m).

The syntheses of complexes **Tb1** and **Dy1** are summarized in Scheme 1.

Synthesis of $\text{Tb}(\text{HPDA})_3 \cdot 4\text{EtOH}(\mathbf{1})$. A mixture of $\text{Tb}(\text{NO}_3)_3 \cdot 5\text{H}_2\text{O}$ (43.5 mg, 0.1 mmol), pyridine-2,6-dicarboxylic acid (34.0 mg, 0.2 mmol), distilled water (2 mL), *N,N*-dimethylformamide (3 mL) and ethanol (1 mL) (pH 2–3) was stirred for



$\text{Ln}=\text{Tb, Dy}$

Scheme 1 Synthesis of lanthanide complexes.

30 min, and then sealed in a 15 mL Teflon-lined reactor, heated at 160 °C for 5 days, and then slowly cooled to room temperature. Well-shaped, light, yellow single crystals of complex **Tb1** suitable for X-ray four-circle diffraction analysis were obtained. Yield: 45.23% (based on Tb). Elemental analysis for $\text{C}_{29}\text{H}_{36}\text{N}_3\text{O}_{16}\text{Tb}$ (M_r : 841.53): Calcd: C, 41.39; N, 4.99; H, 4.31%. Found: C, 41.64; N, 4.74; H, 4.46%. IR (KBr, cm^{-1}): 3545(s), 2990(s), 2776(s), 2420(m), 1623(vs), 1463(m), 1429(vs), 1388(vs), 1278(m), 1191(m), 1077(m), 1020(s), 917(m), 777(m), 734(s), 700(m), 665(m).

Synthesis of $\text{Dy}(\text{HPDA})_3 \cdot 4\text{EtOH}(\mathbf{2})$. The procedure was the same as that for **Tb1** except that $\text{Tb}(\text{NO}_3)_3 \cdot 5\text{H}_2\text{O}$ was replaced by $\text{Dy}(\text{NO}_3)_3 \cdot 5\text{H}_2\text{O}$ (43.8 mg, 0.1 mmol). Yield: 68% (based on Dy). Elemental analysis for Dy1 : $\text{C}_{29}\text{H}_{36}\text{N}_3\text{O}_{16}\text{Dy}$ (M_r : 845.11): Calcd: C, 34.03; N, 5.67; H, 1.56%. Found: C, 34.08; N, 5.71; H, 1.59%. IR (KBr, cm^{-1}): 3566(s), 2988(s), 2776(s), 2420(m), 1635(vs), 1462(m), 1426(vs), 1387(vs), 1278(m), 1191(m), 1020(s), 917(m), 777(s), 735(s), 679(m), 666(m).

Characterization

Infrared spectra were obtained from KBr pellets on a Nicolet Avatar-360 Infrared spectrometer in the 4000–400 cm^{-1} region. Elemental analyses were performed on a Perkin-Elmer 240c element analyzer. The single-crystal X-ray diffraction data for complexes **Tb1** and **Dy1** were collected on a Rigaku R-Axis RAPID IP or a Siemens SMART 1000 CCD diffractometer equipped with graphite-monochromated $\text{Mo K}\alpha$ radiation ($\lambda = 0.71073 \text{ \AA}$), operating at $293 \pm 2 \text{ K}$. The structures were solved by direct methods and refined by full-matrix least-squares based on F^2 using the SHELXTL 5.1 software package. All non-hydrogen atoms were refined anisotropically. Hydrogen atoms were fixed at calculated positions and refined by using a riding mode. Crystal data and details of the data collection and the structure refinement are given in Table 1. Selected bond lengths and angles of complexes **Tb1** and **Dy1** are listed in Table S1 and S2, respectively.†

Photoelectrochemical measurements. The sample was sandwiched between two FTO glass electrodes. Optically transparent electrodes were made from an F-doped SnO_2 -coated glass plate (FTO, 90% transmittance in the visible, $15 \Omega^{-1}$ per square) purchased from Geao Equipment Company, Wuhan, China. The sensitizations were chosen N719 (*cis*-bis(isothiocyanato)bis(2,2-bipyridyl-4,4-dicarboxylato)-ruthenium(II) bis-tetrabutylammonium, or $\text{RuL}_2(\text{NCS})_2 \cdot 2\text{TBA}$ (L = 2,2-bipyridyl-4,4-dicarboxylic acid TBA = tetrabutylammonium, Solaronix Company, Switzerland) at a concentration of $3 \times 10^{-4} \text{ M}$ in pure ethanol solution,

Table 1 Crystal data and structure refinement for complexes **Tb1** and **Dy1**

Data	Dy1	Tb1
Formula	C ₂₉ H ₃₆ N ₃ O ₁₆ Dy	C ₂₉ H ₃₆ N ₃ O ₁₆ Tb
<i>F_w</i>	845.11	841.53
Crystal system	Orthorhombic	Orthorhombic
Space group	<i>Pbcn</i>	<i>Pbcn</i>
<i>a</i> (Å)	16.947(3)	16.967 (1)
<i>b</i> (Å)	10.654(2)	10.672 (1)
<i>c</i> (Å)	18.659(4)	18.648(1)
α (°)	90.00	90
β (°)	90.00	90
γ (°)	90.00	90
Volume (Å ³)	3368.9(12)	3376.4(4)
<i>Z</i>	4	4
<i>D</i> _{calcd} , mg m ⁻³	1.666	1.655
μ , mm ⁻¹	2.296	2.172
<i>F</i> (000)	1700	1696
θ range for data collection	3.14° to 27.46°	2.18° to 25.72°
Limiting indices	-21 ≤ <i>h</i> ≤ 21 -13 ≤ <i>k</i> ≤ 13 -23 ≤ <i>l</i> ≤ 24	-20 ≤ <i>h</i> ≤ 17 -13 ≤ <i>k</i> ≤ 12 -16 ≤ <i>l</i> ≤ 22
Absorption correction		
Data/restraints/parameters	3839/1/227	3208/0/223
Goodness-of-fit on <i>F</i> ²	0.962	0.967
Final <i>R</i> indices [<i>I</i> > 2σ(<i>I</i>)]		
<i>R</i> ₁ ^{<i>a</i>}	0.0351	0.0482
w <i>R</i> ₂ ^{<i>b</i>}	0.0887	0.1211
<i>R</i> indices (all data)		
<i>R</i> ₁ ^{<i>a</i>}	0.0475	0.0538
w <i>R</i> ₂ ^{<i>b</i>}	0.0962	0.1248

$$^a R_1 = \sum \|F_o\| - |F_c| / \sum \|F_o\|, \quad ^b wR_2 = [\sum [w(F_o^2 - F_c^2)^2] / \sum [w(F_o^2)^2]]^{1/2}.$$

and prepared a co-sensitization dye of three lanthanide complexes with the form of single crystals in the same way. The electrolyte used in this work was 0.5 M LiI + 0.05 M I₂ + 0.1 M *tert*-butyl pyridine in 1 : 1 (volume ratio) acetonitrile–propylene carbonate. The films were immersed in 3 × 10⁻⁴ M pure ethanol solutions of **Tb1** or **Dy1** for 2 h, then immersed in 3 × 10⁻⁴ M pure ethanol solutions of N719 for 12 h. Photovoltaic performance was measured by using a mask with an aperture area of 0.2 cm² and the irradiance of sunlight was 100 mW cm⁻².

Based on the *J*-*V* curve, the fill factor (FF) is defined as:

FF = (*J*_{max} × *V*_{max}) / (*J*_{sc} × *V*_{oc}), where *J*_{max} and *V*_{max} are the photocurrent density and photovoltage for maximum power output and *J*_{sc} and *V*_{oc} are the short-circuit photocurrent density and open-circuit photovoltage, respectively. $\eta = (FF \times J_{sc} \times V_{oc}) / P_{in}$ for the overall energy conversion efficiency (*P*_{in} is the power of incident light).

The electrochemical impedance spectroscopy (EIS) of cell measurements were set at a working electrode potential of 550 mV, over a frequency range of 0.1–100 000 Hz. Potential values are referenced with respect to the saturated calomel reference electrode (SCE). Glassy carbon and platinum electrodes were used as the working electrodes and a platinum wire was employed as the counter electrode. A solution of 0.1 M tetrabutylammonium hexafluorophosphate (TBAPF₆, Fluka, electrochemical grade) in CH₂Cl₂ (Aldrich, anhydrous, 99.8%) was used as the supporting electrolyte. A mixed solvent system was employed to prevent adsorption to the electrode. Analyte concentrations of typically 1 mM were used.

Method of calculation

In this work, the three parameter hybrid method proposed by Becke¹⁹ was used with the gradient corrected functional of Lee *et al.* The central metal atoms were treated and the SDD basis set was used to determine the geometry. The non-metallic atoms, oxygen, carbon and hydrogen, were treated by the 3-21G** basis set of double zeta quality plus p, polarization function, in hydrogen atoms and d functions in oxygen and carbon atoms. The calculation method used as well as the basis sets are included in the GAUSSIAN 03 package. The orbital are labeled by the principal and the orbital quantum numbers of the atom. A valence basis set consists of all valence atomic orbitals, occupied or unoccupied, up to the shell of the principal quantum number of highest occupied valence electrons.

Results and discussion

Crystal structures

The single-crystal XRD analyses revealed that compounds **Tb1** and **Dy1** have the same structure. The local coordination environment around Ln³⁺ in compound **Tb1** is depicted in Fig. 1. Both coordination complexes **Tb1** and **Dy1** crystallized into orthorhombic symmetry with space group *Pbcn*. The asymmetric molecular unit of complex **Tb1** contains one distinct Tb³⁺ ion, three HPDA ligands, and four EtOH, as shown in Fig. 1. Tb³⁺ ion is nine-coordinated by six carboxylate oxygen atoms (O_{COO}-) and three pyridine ring N atoms from three neighboring HPDA ligands. The HPDA ligand adopted the coordination type as shown in Fig. 1, in which the metal ion is a Tb³⁺ cation. Moreover, the adjacent units are connected through hydrogen bonding and π–π stacking interaction to form a 3D supramolecule, which makes the framework of complex **Tb1** very stable.

Photoelectrochemical analysis

The lanthanide complexes were assembled onto a nanocrystalline TiO₂ film to prepare a complex/N719 co-sensitized photoelectrode for dye-sensitized solar cell application. Fig. 2 is the surface photovoltage spectrum (SPS) of the photoanodes with a single sensitizer and co-sensitizer. There are two mechanisms emerging in the enhancement of the solar cells. The first process involves the energy levels of N719 and **Ln1**, in which photo-induced electrons of excited complexes inject into the conductive band of TiO₂ easily. The second one is the down-conversion process, in which complexes produce emission under

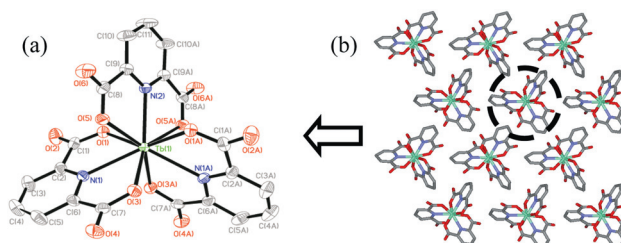


Fig. 1 (a) Molecular structural unit of **Tb1** and (b) perspective view of the packing seen along [010] of **Tb1**.

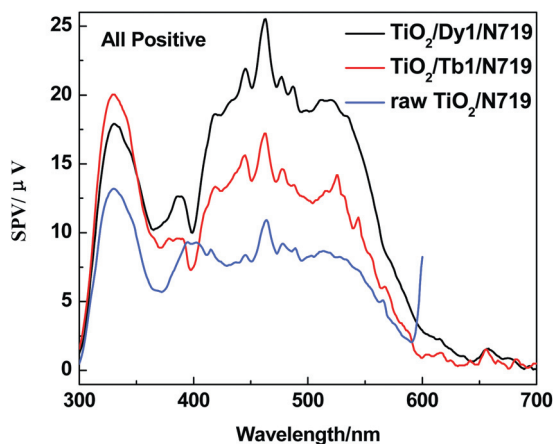


Fig. 2 The relational SPS of composite photoanodes.

illumination, so that the lower energy emission light would be absorbed by N719 to extend the absorption region of the photoanode. With the SPS method, both processes coexist and cooperate. The curves in Fig. 2 indicated that co-sensitizing could enhance the photoelectric signal between 400 and 600 nm. The photovoltage signal increased with **Dy1**, **Tb1**, TiO_2 , which indicated that the separate efficiency of electrons and holes correlate strongly with **Dy1**, **Tb1**, TiO_2 . On the other hand, visible light response range broadened from 400 to 600 nm with **Dy1**, **Tb1**, TiO_2 . The results show that the composite TiO_2 is beneficial for extending the absorption region after co-sensitization in DSSC photoelectrodes. The improvement of composite photoanode co-sensitized by **Dy1** is more evident than **Tb1**.

Fig. 3 presents the performance of the DSSCs in terms of J_{sc} and V_{oc} of co-sensitized solar cells. The result indicates that the photochemical performance of co-sensitized photoelectrodes has been enhanced. Our earlier work indicated that d^{10} metal coordination complexes could affect the photochemical performance of DSSCs due to proton number.¹⁸ In the present work, the co-sensitized photoelectrode has more protons in the central metal of the complex, so that the performance of DSSCs improved. Dy possesses a higher proton number than Tb, and the results coincide with the conclusion reported before¹⁸ (Table 2). The photochemical performance results indicated that the co-sensitized solar cells based on $\text{TiO}_2/\text{Ln1}/\text{N719}$ electrode yielded a remarkably high photocurrent density (J_{sc}), open circuit voltage (V_{oc}) and energy conversion efficiency under standard global AM1.5 solar irradiation conditions. The conversion of the $\text{TiO}_2/\text{Tb1}/\text{N719}$ DSSC system increases by 44% compared with the ones using single organic N719 sensitizers. The $\text{TiO}_2/\text{Dy1}/\text{N719}$ system even shows a greater efficiency, which is 72% higher than that of single-DSSC.

As shown in Table 2, the performances of $\text{TiO}_2/\text{Ln1}/\text{N719}$ composite photoelectrodes were relatively better than that for DSSCs with single organic sensitizers. Table 2 indicated that the cell performance of DSSCs co-sensitized by a mixture of lanthanide complex and N719 were improved. And the co-sensitized DSSCs with **Dy1** showed a better performance than that with **Tb1**. As the proton number of the central metal atom in the lanthanide complexes increased, the efficiency of the DSSCs co-sensitized by **Ln1}/\text{N719} increased.**

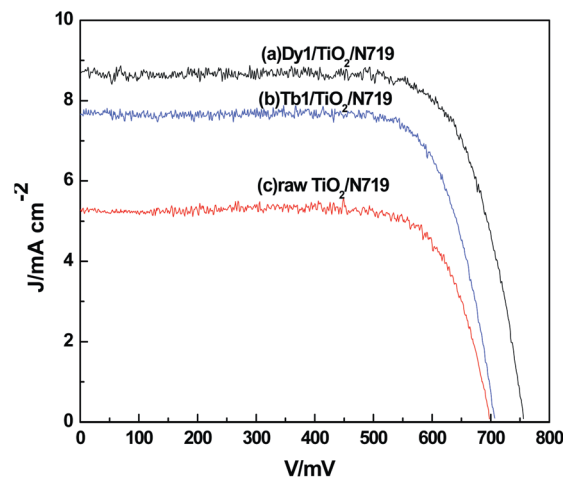


Fig. 3 J - V (current density–voltage) curves for the sunlight-illuminated dye-sensitized solar cells with different lanthanide ligand complexes.

Table 2 Comparison of J - V performance between $\text{TiO}_2/\text{Ln1}/\text{N719}$ and raw TiO_2 photoelectrodes

Photoelectrode	V_{oc}/mV	$J_{sc}/\text{mA cm}^{-2}$	FF	$\eta/\%$
Raw TiO_2	0.698	5.27	0.74	2.86
Tb1}/\text{TiO}_2	0.707	7.75	0.75	4.13
Dy1}/\text{TiO}_2	0.756	8.75	0.78	4.91

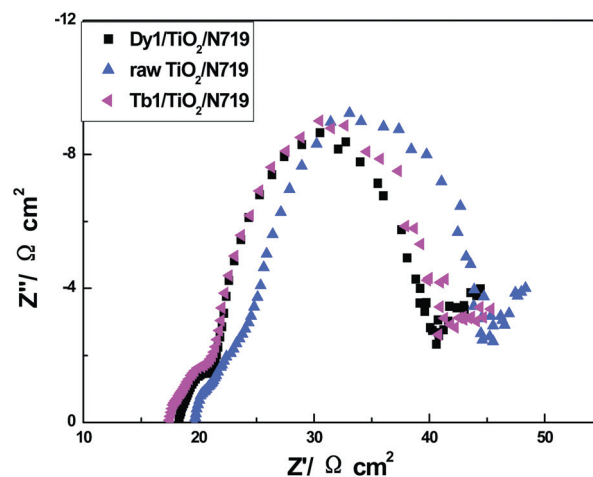


Fig. 4 Nyquist plots of the lanthanide complex/N719 co-sensitized DSSC in standard global AM1.5 solar irradiation.

Electrochemical impedance spectroscopy (EIS)

Fig. 4 presented the Nyquist plots of the lanthanide complex/N719 co-sensitized DSSC under standard global AM1.5 solar irradiation. The results revealed charge carrier dynamics in the interior and interfacial regions of solid–liquid layers, and the effects of mixed sensitizers in composite photoelectrodes. Each curve contains three arcs that are representative for the resistance states of different interfaces. The first arc in the high frequency (>1000 Hz) of the Nyquist plot was assigned to the

electron transfer process at the electrolytes/counter electrode (CE) interface. This feature arose from an increase in the electron transport resistance of the TiO_2 film due to the increase of electron concentration. The electron transport process and charge recombination dominated the impedance spectra in the intermediate frequency range (from 100 to 1000 Hz). The increase of the semicircle radius in the Nyquist plot indicates a reduction in the interfacial charge recombination rate due to the decrease in the conduction band electron concentration. The Warburg diffusion impedance for holes transport in electrolytes could be observed in the low frequency range (less than 1 Hz). In accordance with this observation, the impedance of composite photoelectrode decreased with the increase of protons in atoms, which is beneficial for the photochemical performance of DSSC.

A physical model has been proposed to understand the complex charge-transfer processes in DSSCs.^{20,21} The equivalent circuit used to model this system was $R_s(Q_1R_1)(Q_2(R_2Z_w))$, representing interfaces in composite solar cells. As shown in Fig. 5, R_s represents series resistance consisted of Ohmic components. The R_1 and R_2 were resistance components forming a parallel circuit with constant elements Q_1 and Q_2 .

The complex impedance plot (Nyquist plot) and fitting data using the equivalent circuit for DSSCs are listed in Table 3. As shown in the data, R_2 estimated from semicircle 2 decreased remarkably with the introduction of **Dy1** or **Tb1**. The series resistance R_2 represents electron transport process and charge recombination impedance in the interfacial regions of $\text{TiO}_2/\text{Ln1}$ composite photoelectrode layer. With increasing protons in lanthanide atoms, the energy of relevant frontier molecular orbital increases, which is beneficial for photoelectron transfer between HOMO and LUMO. Therefore, the photochemical performance of co-sensitization of composite TiO_2 photoelectrodes increased compared with single phase TiO_2 . With the increase of the semicircle radius in the Nyquist plot, a reduction in the interfacial charge recombination rate emerged due to the decrease of electron concentration in the conduction band. Hence, we concluded that the intermediate frequency semicircle 2 originated from $\text{TiO}_2/\text{Ln1}$ composite photoelectrodes, which behaved like an n-type inorganic semiconductor. The results also

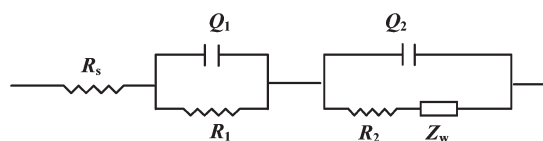


Fig. 5 Equivalent circuit in composite solar cells composed of FTO| $\text{TiO}_2/\text{Ln1}$ -dye| I_3^-/I^- ||Pt|FTO. (Component explanation: R_s = series resistance, R_1 , R_2 = the charge-transfer resistance, Q_1 , Q_2 = the symbol for the constant phase element, and Z_w = Warburg impedance).

demonstrated that co-sensitization in TiO_2 could utilize more UV-visible light than DSSCs containing individual dyes (Table 2).

Relationship between structures and electrochemical properties

The geometric and electronic structures of the sensitizer are the key factors for solar cells, which determine related electrochemical properties. Crystal structural analyses revealed that compounds **Tb1** and **Dy1** are isostructural (see ESI†). Their unit cell dimensions, volumes, related bond distances and bond angles differ only slightly. In the coordination polyhedron around Ln, the N1, N2 and N3 atoms came from three phenyl rings. This is one of the common coordination patterns for complexes with a coordination number of nine. As shown in Fig. 1, there are three independent planes of phenyl rings, which orient approximately orthogonally to the plane of the three coordinated nitrogen atoms. The dihedral angles between the two phenyl rings increase with the proton number, and the distance from Ln atom to the coordination plane also increases. This induced more electrons transferring across the same plane due to the enlarged space.

The bond distances can be divided into two different types presented in the coordination sphere of the RE metal. The Ln–O bond distances are 2.425(5) Å for **Tb1** and 2.343(7) Å for **Dy1**, and the Ln–N bond distances are 2.515(5) Å (**Tb1**) and 2.495(5) Å (**Dy1**), respectively. The O–Ln–O bond angles range from 127.7° (**Tb1**) to 128.2° (**Dy1**), and the O–Ln–N bond angles range from 120.2° (**Tb1**) to 120.7° (**Dy1**). The data indicated that the Ln–N and Ln–O bonds in **Dy1** are more stable compared to **Tb1**. These bond distances and bond angles are comparable to the values in other lanthanide complexes. Interestingly, the N–Ln–N bond angles are nearly 120°, and the Ln atoms are located in the center of the N_3 equilateral triangles. Adjacent HPDA groups in three neighboring layers of coordination complexes are parallel and the distance between two neighboring parallel layers is around 3.257 Å, which indicates π - π stacking interactions. Fig. 6 shows the packing diagram of **Ln1** along the *c*-axis. Hydrogen bonds are indicated by dashed lines. Some observed hydrogen bond interactions in coordination complexes are given in Table 4. The data showed that the hydrogen bond lengths are in the following order: $\text{Dy}_{\text{O}\dots\text{H}} > \text{Tb}_{\text{O}\dots\text{H}}$. Therefore, a 3D supramolecular structure is formed through π - π stacking interaction and hydrogen bonding interactions between the carboxyl groups. There is a large void between the layers in the complex.

From their electrochemical properties (data in Table 2) it can be concluded that the electron-donating capability is better in a stable single molecule structure. Generally speaking, the decrease of the bond length and the deviation distance are

Table 3 Parameters obtained by fitting the impedance spectra of composite solar cells using the equivalent circuit

Sample	R_s/Ω	$\text{CPE}_1(Y_{\text{O}_2}/\text{Fs}^{n-1})$	n_1	R_1/Ω	$Z_w(Y_{\text{O}_1}/\text{S})$	R_2/Ω	$\text{CPE}_2(Y_{\text{O}_2}/\text{Fs}^{n-1})$	n_2
TiO_2	19.45	1.532×10^{-3}	0.542	6.756	0.2057	17.94	6.77×10^{-4}	0.943
Tb1	17.46	9.154×10^{-4}	0.914	19.39	0.2346	4.251	5.509×10^{-4}	0.800
Dy1	18.36	6.739×10^{-4}	0.934	18.14	0.201	3.143	1.663×10^{-3}	0.810

advantageous for electrochemical reactions, while the enlargement of the space between the layers leads to superior cell performance.

Molecular orbitals and band structure calculations of lanthanide complex

In order to further understand the energy band structure in lanthanide complex, we performed *ab initio* calculations for the molecular orbitals based on the time-dependent density functional theory (TD-DFT) with 3-21G** basis set. The geometric parameters obtained from X-ray diffraction analyses were fully optimized in conjunction with the solid model. The MO diagram for $\text{Ln}(\text{HPDA})_3 \cdot 4\text{EtOH}$ ($\text{Ln} = \text{Tb}, \text{Dy}$), is shown in Fig. 7, which presented the typical pattern of frontier molecular orbital in lanthanide complexes for f orbitals. The three ligand extremes differ in the number of electrons: two adopted the neutral form, while another was described as anionic according to the electron count based on X-ray diffraction analyses on the single crystal structure. These results included the highest occupied (HOMO) and the lowest unoccupied (LUMO) molecular orbitals for each cluster. The molecular skeletons were shown as ball-stick models (see ESI†).

For each cluster, the occupied FMO levels were found to be very close to each other within 0.13 eV, and the same for the unoccupied FMO levels. The occupied and unoccupied FMOs related to the valence and conduction bands in the case of bulk complexes.

In Table 4, some useful electronic properties are listed for the stable clusters, such as the HOMO energy level (E_{H}) and LUMO energy level (E_{L}). The E_{HL} value of bulk TiO_2 is around 3.05 eV according to the literature.²² As shown in Fig. 7, sensitization of

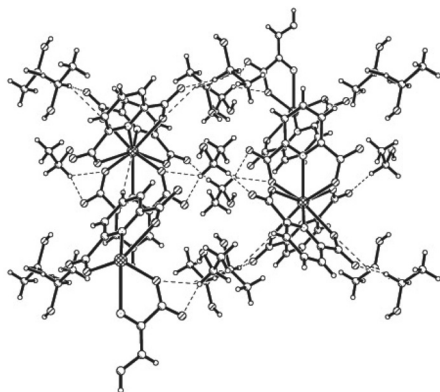


Fig. 6 The unit of complex **Tb1** extends into a 3D supramolecular by O–H...O hydrogen bonds along the [001] direction.

Titania to visible light through electron transfer from lanthanide complex to anatase nanocrystals. Specifically, the E_{HL} values of lanthanide complex were very close to that of bulk TiO_2 . Additional photoluminescent and electrochemical properties could prove the same results as $\text{Tb(III)} < \text{Dy(III)}$. The calculated energy levels for complex Tb(III) and Dy(III) agreed well to the experimental results. The E_{HL} of complex Dy(III) was closer to TiO_2 than that of complex Tb(III) . And the gap between E_{LUMO} of complex Dy(III) and E_{CB} of TiO_2 was smaller, which could mean that it is easier to inject electrons into the conduction band of TiO_2 during the transfer process. Furthermore, the gap between electrolyte and the E_{HOMO} of Dy(III) is smaller than that of Tb(III) , leading to easier transfer from electrolyte to Dy(III) .

Conclusions

In conclusion, two lanthanide complexes with pyridine-2,6-dicarboxylic acid ligands have been synthesized under hydrothermal or solvothermal conditions. Complexes have mononuclear structures and self-assemble to form a 3D supramolecular structure through hydrogen bond and aromatic π - π interactions between adjacent metal-organic complex coordination chains. Both nine-coordinate lanthanide metal complexes were attached to a nanocrystalline TiO_2 film to assemble co-sensitized photoelectrodes with N719 for dye-sensitized solar cells, which yielded a remarkably high optoelectronic efficiency of 4.91%. Moreover, the V_{oc} and I_{sc} increased after introducing the cosensitizers. It is worth mentioning that this is the first time that 2,6-bis(imino)pyridyl types of lanthanide inorganic coordinate complexes co-sensitized with N719 in TiO_2 have been used

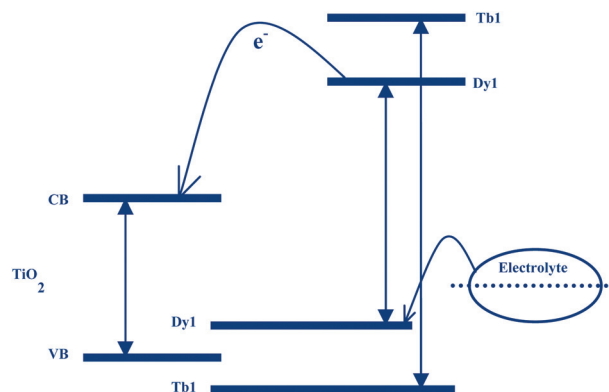


Fig. 7 Schematic energy diagrams showing proposed electron and energy transfer mechanisms in composite photoelectrode of titania-based lanthanide complexes (VB = valence band; CB = conduction band).

Table 4 Comparison of the bond lengths and angles in the molecular structure of the lanthanide complexes

Bond lengths of Ln–O/Å	Bond lengths of Ln–N/Å	O–Ln–O bond angles/°	N–Ln–N bond angles/°	Distance of Ln deviated away from the coordination plane/Å	Dihedral angles between pyridine rings plane/°	Hydrogen bond lengths/Å	Electron structure of Ln	$E_{\text{HOMO}}/\text{eV}$	$E_{\text{LUMO}}/\text{eV}$
Tb1 2.425(5)	2.515(5)	127.7(2)°	120.2(2)°	0.0105	89.06	3.080	$[\text{Xe}]4f^8 6s^2$	2.4768	5.909
Dy1 2.343(7)	2.495(5)	128.2(14)°	120.7(3)°	0.0665	89.13	3.439	$[\text{Xe}]4f^9 6s^2$	2.5394	5.894

to form composite photoelectrodes. On the other hand, it has been shown that the optoelectronic efficiency can be strongly increased through postsynthesis functionalization of titania using visible light sensitizing species, for example, grafting of dye molecules or depositing narrow band gap semiconductor nanocrystals onto premade titania matrixes. Undoubtedly, they play an important role in the optimization matching with dyes for increasing electricity conversion efficiencies in compounds. More importantly, it demonstrates a way to design more sophisticated and appropriate dye structures to satisfy the needs of DSSC technology.

Acknowledgements

This work was supported by the National Science Foundation of China (Grant No. 20971031, 21071035 and 21171044), the China Postdoctoral Science Foundation Funded Project (No. 65204), and the key Natural Science Foundation of the Heilongjiang Province, China (No. ZD201009).

Notes and references

- 1 B. O'Regan and M. Grätzel, *Nature*, 1991, **353**, 737.
- 2 H. Choi, I. Raabe, D. Kim, F. Teocoli, C. Kim, K. Song, J. Yum, J. Ko, Md. K. Nazeeruddin and M. Grätzel, *Chem.–Eur. J.*, 2010, **16**, 1193.
- 3 C. Chen, Y. Hsu, H. Chou, K. R. Justin Thomas, J. T. Lin and C. Hsu, *Chem.–Eur. J.*, 2010, **16**, 3184.
- 4 D. Kuang, T. Brezesinski and B. Smarsly, *J. Am. Chem. Soc.*, 2004, **126**, 10534.
- 5 A. Ehret, L. Stuhl and M. T. Spitler, *J. Phys. Chem. B*, 2001, **105**, 9960.
- 6 Y. S. Chen, Z. H. Zeng, C. Li, W. Wang, X. S. Wang and B. W. Zhang, *New J. Chem.*, 2005, **29**, 773.
- 7 M. Guo, P. Diao, Y. J. Ren, F. S. Meng, H. Tian and S. M. Cai, *Sol. Energy Mater. Sol. Cells*, 2005, **88**, 23.
- 8 X. F. Wang, Y. Koyama, O. Kitao, Y. Wada, S. Sasakie, H. Tamiaki and H. Zhou, *Biosens. Bioelectron.*, 2010, **25**, 1970.
- 9 B. A. Andreev, Z. F. Krasilnik, D. I. Kryzhkov, V. P. Kuznetsov, T. Gregorkiewicz and W. Jantsch, *Appl. Phys. Lett.*, 2006, **88**, 201101.
- 10 M. Abdullah, T. Morimoto and K. Okuyama, *Adv. Funct. Mater.*, 2003, **13**, 800.
- 11 D. J. Zhang, T. Y. Song, J. Shi, W. R. Yin, P. Zhang, L. Wang, Y. Wang, K. R. Ma, Y. Fan and J. N. Xu, *Inorg. Chem. Commun.*, 2007, **10**, 1067.
- 12 N. Wang, S. Yue, Y. Liu, H. Yang and H. Wu, *Cryst. Growth Des.*, 2009, **9**, 368.
- 13 G. B. Che, C. B. Liu, B. Liu, Q. W. Wang and Z. L. Xu, *CrystEngComm*, 2008, **10**, 184.
- 14 P. Mahata and S. Natarajan, *Inorg. Chem.*, 2007, **46**, 1250.
- 15 T. Whitfield, L. M. Zheng, X. Wang and J. J. Allan, *Solid State Sci.*, 2001, **3**, 829.
- 16 M. S. Liu, Q. Y. Yu, Y. P. Cai, C. Y. Su, X. M. Lin, X. X. Zhou and J. W. Cai, *Cryst. Growth Des.*, 2008, **8**, 4083.
- 17 L. Yoann, M. B. Dario, J. Gediminas and D. M. Nathan, *J. Am. Chem. Soc.*, 2007, **129**, 8688.
- 18 X. Wang, Y. Yang, R. Fan and Z. Jiang, *New J. Chem.*, 2010, **34**, 2599.
- 19 D. G. Truhlar, B. C. Garrett and S. J. Klippenstein, *J. Phys. Chem.*, 1996, **100**, 12771.
- 20 K. Mukherjee, T. H. Teng, R. Jose and S. Ramakrishna, *Appl. Phys. Lett.*, 2009, **95**, 012101.
- 21 J. E. Trancik, S. C. Barton and J. Hone, *Nano Lett.*, 2008, **8**, 982.
- 22 Z. W. Qu and G. J. Kroes, *J. Phys. Chem. C*, 2007, **111**, 16808.